Environmental Science: Atmospheres

ROYAL SOCIETY OF CHEMISTRY

PAPER

View Article Online
View Journal | View Issue

Cite this: *Environ. Sci.: Atmos.*, 2025, **5**, 300

Photodegradation of naphthalene-derived particle oxidation products†

Félix Sari Doré, ‡[a] Cecilie Carstens, [a] Jens Top, [b] Yanjun Zhang,[a] Clément Dubois, §[a] Sébastien Perrier,[a] Imad El Haddad, [b] David M. Bell *[b] and Matthieu Riva *[a]

While photochemical aging is known to alter secondary organic aerosol (SOA) properties, this process remains poorly constrained for anthropogenic SOA. This study investigates the photodegradation of SOA produced from the hydroxyl radical-initiated oxidation of naphthalene under low- and high-NO_x conditions. We used state-of-the-art mass spectrometry (MS) techniques, including extractive electrospray ionization and chemical ionization MS, for the in-depth molecular characterization of gas and particulate phases. SOA were exposed to simulated irradiation at different stages, *i.e.*, during formation and growth. We found a rapid (*i.e.* >30 min) photodegradation of high-molecular-weight compounds in the particle-phase. Notably, species with 20 carbon atoms (C_{20}) decreased by 2/3 in the low-NO_x experiment which was associated with particle mass loss (~12%). Concurrently, the formation of oligomers with shorter carbon skeletons in the particle-phase was identified along with the release of volatile products such as formic acid and formaldehyde in the gas-phase. These reactions are linked to photolabile functional groups within the naphthalene-derived SOA products, which increases their likelihood of being degraded under UV light. Overall, photodegradation caused a notable change in the molecular composition altering the physical properties (*e.g.*, volatility) of naphthalene-derived SOA.

Received 4th September 2024
Accepted 6th January 2025

DOI: 10.1039/d4ea00125g

rsc.li/esatmospheres

Environmental significance

Naphthalene is a major anthropogenic volatile organic compound (VOC) and an important contributor to secondary organic aerosol (SOA) formation in urban environments. However, the evolution of the chemical composition of naphthalene-derived SOA remains uncertain. In this study, SOA were generated from the OH-initiated oxidation of naphthalene and exposed to UV radiation to investigate the influence of photochemical aging on the chemical composition. We observed that photodegradation induced a loss of SOA mass and high-molecular-weight dimers that resulted in the production of smaller unsaturated dimers and the emission of volatile species into the atmosphere. These observations underline the importance of photochemistry on urban SOA physicochemical properties and lifetime.

Introduction

Organic aerosols (OA) are nefarious to human health,[1–3] influence the global climate by scattering and absorbing solar radiation,[4,5] and modify the lifetime and albedo of clouds by acting as cloud condensation nuclei.[6–10] OA are a key component of atmospheric aerosols and account for 20 to 90% of the tropospheric submicron aerosol mass.[11,12] The OA sources include anthropogenic sources; *i.e.*, traffic emissions, industrial activities, energy production,[13,14] and biogenic sources such as biomass burning and emissions from vegetation.[15–18]

From these important emission sources, the oxidation of volatile organic compounds (VOCs) leads to oxidation products of lower volatility than the precursor VOC and greatly participates in SOA formation and growth. This growth occurs either by the reaction of an oxidized gas molecule with a particle after collision (*i.e.*, reactive uptake),[19,20] by absorptive partitioning[21,22] or by the condensation of low-vapor pressure compounds.[12,18,23,24] Due to the importance of SOA on our environment and health, investigating the chemical processes involved in SOA growth and aging is necessary, especially given that organic species experience substantial chemical changes over their lifetime (usually a couple of days).[25]

[a]*Université Claude Bernard Lyon1, CNRS, IRCELYON, UMR 5256, 69100 Villeurbanne, France*

[b]*PSI Center for Energy and Environmental Sciences, Paul Scherrer Institute, Villigen, Switzerland*

† Electronic supplementary information (ESI) available. See DOI: https://doi.org/10.1039/d4ea00125g

‡ Present address: Department of Chemistry and Molecular Biology, Atmospheric Science, University of Gothenburg, SE-41390, Gothenburg, Sweden.

§ Present address: Department of Chemistry, Aarhus University, DK-8000, Aarhus C, Denmark.

SOA aging is influenced by a variety of chemical processes, such as oxidative processes, (*e.g.* heterogeneous oxidation from ozone (O_3), N_2O_5, or hydroxyl radicals (OH), which can be formed in the aerosol itself),[26] or non-oxidative processes, *e.g.*, hydrolysis, aldolisation, esterification, peroxyhemiacetal/hemiacetal formation.[27,28] These chemical reactions lead to different outcomes (*e.g.*, fragmentation, functionalization, or oligomerization) in the condensed phase.[12,29] Such changes not only alter the SOA chemical composition but also ultimately influence their optical and physical properties (*e.g.*, volatility, hygroscopicity, viscosity).[30–32] Functionalization and oligomerization tend to decrease the volatility of the molecules by increasing their polarity or carbon number, thus changing their lifetime in the aerosol phase. Fragmentation and carbon bond cleavage result in higher vapor pressure products, which can cause a reduction of the SOA mass if fragmentation continues unabated.[31,33] Photochemical processes have also been shown to greatly impact the SOA chemical composition during aging,[34–38] and are hypothesized to be a key driver of SOA physicochemical properties. More specifically, previous work showed that photochemical aging of biogenic-derived SOA alters their morphology from well-mixed fresh to phase-separated aerosols.[39] This process may be caused by an increase in oligomer content increasing particle viscosity. In addition to impacting SOA composition and morphology, photodegradation is a major SOA removal mechanism that needs to be considered.[30,40–44] This mass loss is associated with the presence of photolabile functional groups that are susceptible to be photodegraded and form volatile species that can outgas from the condensed phase. Among them, organic peroxides and carbonyls represent an important fraction of the SOA mass[45–50] and have been identified as photochemically active species.[40,42–44] Krapf *et al.*[40] suggested that carbonyls determine the photolability of α-pinene SOA rather than peroxides while Pospisilova *et al.*[30] showed that moderately oxygenated molecules are the most photolabile species. These uncertainties underline the need to perform additional investigations on the SOA evolution under various environmental conditions.

In urban atmospheres, polycyclic aromatic hydrocarbons (PAHs) represent an important group of anthropogenic precursors capable of forming SOA.[51–54] Composed of fused aromatic rings, PAHs can be rapidly oxidized by the different atmospheric oxidants, predominantly OH radicals.[55–59] PAH-derived SOA are also known to constitute a considerable health hazard because of their deleterious effect on human health (carcinogenic, embryotoxic, oxidative potential).[2–4,60–64] Studies have shown that PAH-derived SOA are sensitive to photochemistry.[65] As a result, evaluating the impact of photodegradation on PAH-derived SOA is important to understand the evolution of aerosol particles notably in urban environments.

In this study, we investigated the formation and evolution of secondary organic aerosol (SOA) produced from the oxidation of naphthalene, one of the most abundant gaseous PAH in the atmosphere,[63,66] by OH radicals under various UV and environmental conditions. Experiments were conducted in a Teflon atmospheric simulation chamber. Gas and particle-phase chemical characterization was achieved using state-of-the-art online mass spectrometry techniques.

Experimental section

Experiments were conducted at the Paul Scherrer Institute in Switzerland in a 9 m^3 atmospheric chamber made of Teflon® fluorocarbon film described by Platt *et al.*[67] They were performed in batch mode (*i.e.*, static), with no dilution once the particle formation started, except during the first part of the low-NO_x experiment, in which an airflow was unintentionally kept open for 2.5 hours before being closed. The container housing the chamber was temperature-regulated and maintained at a temperature of 24 °C (±2 °C). The chamber was flushed overnight at a flow rate of 35 standard liter per minute (SLPM) with dry purified air obtained from an AADCO (AADCO 250 series, AADCO Instruments, Inc., USA) system. At the start of the experiments, humid air was produced by bubbling dry clean air through ultrapure water. Several instruments were used to monitor the experimental conditions. O_3 was obtained by passing pure air over a UV light source inside a stainless-steel cylinder and was measured by a UV photometric O_3 analyzer (model 49C, Thermo). A dew point hygrometer (SC-05, Rotronic) was used to monitor the temperature and relative humidity (RH). NO_x concentrations were not available, but significant differences in NO_x levels were expected depending on the OH production process. OH radicals were produced within the chamber by either the ozonolysis of tetramethylethylene (TME) (IUPAC name: 2,3-dimethyl-2-butene), a reaction yielding OH, HO_2 radicals and acetone with low NO_x levels,[68] or by the photolysis of nitrous acid (HONO), resulting in OH radicals and nitric oxide (NO).[69] In the dark experiment, NO_x concentrations would remain below limit of detection since there was no NO_x injections into the chamber. Historically, generating OH radicals with HONO results in NO_x concentrations below 2 ppb without the injection of either NO or NO_2.[69,70] Photodegradation was initiated using a bank of black light (set of 40 Cleo Performance solarium lamps from Philips with a power of 90–100 W each, emission spectrum available in Fig. S1†). Another study using this chamber estimated the UV-A lights J_{NO_2} to be 3×10^{-3} s^{-1}.[30] OH radical concentrations were estimated by monitoring the decay of butanol-d9 (1 μL–30 ppb) as previously described by Barmet *et al.*[71] Naphthalene was injected into the chamber by passing an airflow through the headspace of solid naphthalene and was monitored with a total hydrocarbon counter (THC monitor APHA-370, Horiba).

The impact of aging and photochemistry-driven aging on naphthalene-derived SOA was investigated by performing two types of experiments: (i) particles grown in the dark before being exposed to the lights, (ii) particles grown with the lights on and aged in the dark. SOA formation in the dark was performed by mixing naphthalene with OH radicals generated from TME ozonolysis, resulting in oxidation under low-NO_x levels. Therefore, this experiment is referred to as the low-NO_x experiment. This experiment was conducted at high relative humidity (RH = 71%) with a concentration of 1.25 ppm and 106 ppb of O_3 and naphthalene, respectively. 10 μL of TME (227 ppb) was injected twice through a septum into a heated line which was flushed with dry air to introduce the VOC into the

chamber. The first injection was diluted by the airflow that remained open. After closing the airflow, the second injection was performed to form more SOA. During the high-NO_x experiment, OH radicals were formed from the photolysis of HONO. This experiment was conducted at high relative humidity (RH ~ 82%) in the presence of 131 ppb of naphthalene with a background level of 0.09–0.1 ppm of O_3. HONO was obtained by passing an airflow through a reactor where both sulfuric acid (H_2SO_4) and sodium nitrite ($NaNO_2$) were added dropwise.[72]

The chemical composition of gaseous species was retrieved with an atmospheric pressure chemical ionization (CI) inlet coupled to a Q-Exactive Orbitrap mass spectrometer (Thermo Scientific, USA), hereafter referred to as CI-Orbitrap, and a Vocus proton transfer reaction time-of-flight mass spectrometer (Vocus 2R PTR-TOF, Tofwerk), later referred to as Vocus. An in-depth description and characterization of the inlet was performed by Riva *et al.*,[73] so the CI inlet was only described succinctly here. A coaxial sample flow of 10 SLPM was supplied to the instrument and was kept in the center of the drift tube by adding a 20–40 SLPM sheath flow controlled by a mass flow controller (MFC) to minimize wall losses. By flushing 2 standard cubic centimeters per minute (sccm) of dry pure air over a 1% liquid ammonia solution, ammonia vapors (NH_3) were generated and mixed with the sheath flow. NH_3 vapors passed through a soft X-ray photoionizer (Hamamatsu, L9491) to generate ammonium ions (NH_4^+). NH_4^+ was chosen as the reagent ion due to its low selectivity (*i.e.*, suitable for a large variety of oxidation products[74]).

The Vocus reagent ion source consisted of a hollow cathode producing a plasma between two conical surfaces.[75] Like the CI-Orbitrap, the Vocus was operated in ammonia mode. The generated NH_4^+ ions entered the focusing ion-molecule reactor (FIMR), which replaced the drift tube of traditional PTR-TOF.[75–79] NH_4^+ ions and the analytes were mixed within the FIMR where adduct ions were formed. Using both instruments allowed us to study compounds with an extended volatility range[74,80] and to be more robust toward possible RH variations. Indeed, the NH_4^+-CI-Orbitrap has exhibited a RH dependence, which was not the case for the Vocus-PTR.[74,75]

Particles in the experiment were monitored using a scanning mobility particle sizer (SMPS, TSI Incorporated, USA) over a 15–638 nm diameter range. Particles were chemically characterized using an extractive electrospray ionization inlet coupled to an atmospheric pressure interface time-of-flight mass spectrometer (APi-TOF, Tofwerk AG, Thun, Switzerland). This instrument was previously described by Lopez-Hilfiker and referred to as EESI-TOF from henceforth.[81] The aerosol flow (0.8–1.0 SLPM) before entering the EESI-TOF went through a multi-channel carbon denuder (Ionicon) to remove >99.9% of gas-phase compounds.[81,82] Periodical blanks (~every 5–15 min) were performed by passing the aerosols through a HEPA filter to obtain a background-corrected signal. The EESI electrospray solution consisted of ultrapure water doped with 100 ppm of sodium iodide (NaI), pushed through an untreated fused silica capillary (360 μm outer diameter, 75 μm internal diameter, BGB Analytik AG, Boeckten, Switzerland) at 100–200 mbar. The fluid flow was controlled by a high-precision pressure regulator (MFCS-EZ 1000 mbar, Fluigent, Inc., Lowell, MA, USA) coupled to the electrospray liquid bottle. 2700–2900 V was applied to ensure spray stability and particle extraction.[81,83] The instrument was operated in positive mode, resulting in the formation of [analyte + Na]$^+$ adduct ions. The EESI-TOF and Vocus signal were normalized using the method detailed in the ESI.†

Results and discussion

Particle formation and growth

Fig. 1 shows the SOA formation and the evolution of the mass concentration and chamber conditions throughout the experiments, with particle densities assumed to be 1.5 g cm^{-3} (Kautzman *et al.* 2010).[84] Both the total SOA mass concentration (orange circles) and the mass loadings for individual particle sizes (color scale) are indicated. An overview of the experimental conditions was compiled in Table S1.† While SOA can form from naphthalene ozonolysis,[85] particles were not observed before the production of OH radicals in both experiments. Presumably, this was due to the weak naphthalene reactivity with ozone. The first injection of TME resulted in particle formation up to ~102 μg m^{-3}. Due to the unintentional dilution flow in the chamber, OH levels were not estimated and SOA mass rapidly decreased. Therefore, a second injection of 10 μL of TME was performed after ~2.75 hours ($t = -1$ hour in Fig. 1A) to increase particle mass, with RH = 33% and 0.6 ppm of O_3 present in the chamber. This second injection resulted in an OH radical concentration of 2.7×10^7 molecules per cm^3, which was significantly higher than tropospheric OH levels (1.1×10^6 molecules per cm^3).[86] This high OH level rapidly increased particle mass concentration to 122 μg m^{-3}. While the first injection raised the number of particles from 646 particles per cm^3 (*i.e.*, background level) to 1.2×10^6 particles per cm^3, the 2nd injection only showed an increase from 5.4×10^4 to 2×10^5 particles per cm^3. This difference indicates that existing particles acted as a condensation sink for gaseous oxygenated species produced from naphthalene oxidation, and inhibited part of the new particle formation. The fast SOA formation from the 1st injection was followed by a significant mass concentration decrease, from ~102 to 42 μg m^{-3} (59% decrease).

The 2nd injection raised the mean mass geometric diameter to ~140 nm, indicating that gaseous species condensed onto preexisting particles instead of participating in new particle formation and allowed to produce sufficient SOA mass to study aging processes. The mean diameter stayed within 140–155 nm for the rest of the experiment. Lights were turned on ~50 min after the second injection for 65 min to study the impact of the photodegradation processes on dark-grown SOA. When lights were turned on, a net decrease of both the mean mass geometric diameter (from 150 to 140 nm) and particle mass concentration (12% loss after wall-loss corrections, details about the correction in Pospisilova *et al.*)[87] was observed. This is indicative that photodegradation led to particle mass reduction due to a release of volatile compounds, as observed in previous studies.[30,41–44]

During the high-NO_x experiment, UV lights were turned on for 1.5 hours. OH radicals concentration reached 4.1×10^8

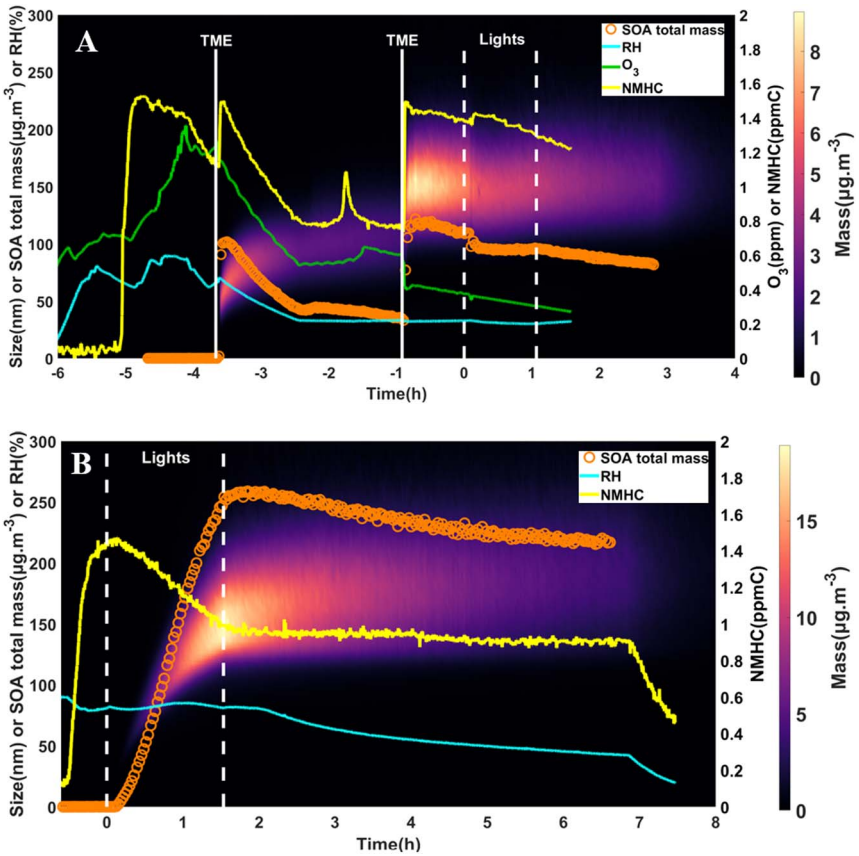

Fig. 1 Evolution of SOA mass concentration measured by the SMPS and chamber conditions for (A) low-NO_x and (B) high-NO_x experiment. The mass loadings of the various sizes of particles are indicated by the color scale. $t = 0$ hours marked the start of the UV lights, and dotted white bars indicate the period when UV lights were turned on. The chamber conditions monitored include the total SOA mass (wall-loss corrected, orange circles), RH (blue), ozone (green), and non-methane hydrocarbon (NMHC, yellow). NMHC was used to monitor the naphthalene concentrations as well as the TME injected. The measurement unit was ppmC, meaning that the real concentrations of naphthalene and TME were respectively 10 times and 6 times lower than what the NMHC suggests.

molecules per cm^3 and up to 1.8×10^5 particles per cm^3 were formed. SOA formation peaked at 254 μg m^{-3}, with a geometric mean diameter of 160 nm. The mass loss associated with photodegradation cannot be observed in this case, as it was overshadowed by the SOA formation. Over the next 5 hours, particles continued to grow due to either the slow condensation of organic vapors or coagulation, and the geometric mean diameter increased by ~20% up to 190 nm.

Gas- and particle-phase species identification

Naphthalene oxidation from OH radicals occurred mostly (~95%) from the OH addition pathway,[88] with the remaining fraction of the reaction taking place through the hydrogen abstraction pathway. The resulting RO_2 radicals were $C_{10}H_7O_y$, $C_{10}H_9O_y$, and $C_{10}H_{11}O_y$, and the main dimers formed from the bimolecular reaction of these RO_2 radicals were $C_{20}H_{16}O_y$, $C_{20}H_{18}O_y$ and $C_{20}H_{20}O_y$.[88–90] The suggested reaction pathways were given in Fig. S2,† and the resulting closed-shell oxidation products observed were compiled in Fig. S3 and Table S2.† The contribution of the oxidation pathways to SOA formation was estimated by comparing the ratios of $C_{10}H_6$ oxidation products (formed through the H abstraction pathway) to $C_{10}H_{10}$ compounds (formed through the OH addition pathway). At the peak of SOA formation of the low-NO_x experiment, particle-phase $\frac{C_{10}H_6}{C_{10}H_{10}}$ ratio amounted to 0.07 while gas-phase $\frac{C_{10}H_6}{C_{10}H_{10}}$ ratio was 0.25, showing that $C_{10}H_{10}$ species were more abundant (relatively to $C_{10}H_6$) in the particle-phase than in the gas-phase. Similar observations from the beginning of SOA formation in the high-NO_x experiment were noted, with particle-phase and gas-phase $\frac{C_{10}H_6}{C_{10}H_{10}}$ amounting to 0.11 and 0.84, respectively. This suggests that species produced from the OH addition pathway partitioned more efficiently towards particle-phase, although it is important to stress that these observations were qualitative.

In the low-NO_x experiment, the SOA chemical composition remained similar across the two injections (Fig. S3-A†). Moreover, most of the gaseous and particulate compounds detected were consistent with what was observed in previous studies on naphthalene oxidation.[52,65,84,91] Table S2† depicts both N-containing and non-N-containing species identified in previous studies. However, to ease the comparison between the

different experiments, this section focuses on the non-N-containing compounds. Important non-N-containing oxidation products were identified such as phthaldialdehyde ($C_8H_6O_2$), 1,4-naphthoquinone ($C_{10}H_6O_2$), and 2-formylcinnamaldehyde ($C_{10}H_8O_2$). Generally, condensed-phase non-N-containing compounds were highly oxidized (*i.e.*, O $\geq$ 4 for monomers and $\geq$6 for dimers), with no visible difference between the low- and high-NO_x conditions. As shown in Fig. S3-A and Table S2,† some of the most abundant particle-phase compounds identified in the low-NO_x experiment included $C_8H_6O_4$ (m/z = 166.026, number 7 in Fig. S3 and Table S2†), $C_{10}H_8O_3$ (m/z = 176.047, number 10), $C_{10}H_8O_4$ (m/z = 192.042, number 13), $C_{10}H_{10}O_3$ (m/z = 178.062, number 11), $C_{10}H_{10}O_4$ (m/z = 194.057, number 14), and $C_{10}H_{10}O_5$ (m/z = 210.052, number 17). The three former compounds ($C_8H_6O_4$, $C_{10}H_8O_3$, and $C_{10}H_8O_4$) were ring-opening products. Contrariwise, $C_{10}H_{10}O_3$ was a ring-retaining product and $C_{10}H_{10}O_4$ and $C_{10}H_{10}O_5$ were also most likely ring-retaining compounds. High-NO_x particulate oxidation products (Fig. S3-C and Table S2†) exhibited a lesser fraction of non-N-containing ring-retaining species, suggested by the larger concentration of $C_{10}H_8O_4$ compared to $C_{10}H_{10}O_4$. The same trend was observed for the gas-phase oxidation products, where $C_{10}H_{10}O_2$ (m/z = 160.052, number 6) dominated in the low-NO_x environment (Fig. S3-B and Table S2†) while $C_{10}H_8O_2$ (m/z = 162.068, number 5) dominated in the high-NO_x environment (Fig. S3-D and Table S2†). These results agree with previous studies,[52,84] which noted a higher relative intensity in gas-phase ring-retaining products for low-NO_x conditions compared to high-NO_x conditions.

EESI signal variations

Fig. S4-A† compares the variation of the wall-loss corrected SOA mass recorded by the SMPS with the evolution of the normalized total signal recorded by the EESI for $C_{8-10}H_xO_y$ and $C_{18-20}H_xO_y$ species during the low-NO_x experiment. The light period caused a 12% loss of the particle mass loadings, while the EESI normalized signal originally did not show a considerable drop. After that, the particle mass remained constant, while the EESI signal continued to decay quickly. A possible explanation can be the dependency of the EESI sensitivity as a function of the particle size. Indeed, as shown by Lee *et al.*[92] the EESI signal depends not only on the mass loading but also on the geometric mean aerosol diameter. This is caused by smaller particles diffusing and coalescing more efficiently with the electrospray droplets, therefore resulting in greater extraction efficiency. However, this effect is mainly important for particles with a diameter lower than 100 nm. In our experiment, naphthalene-derived SOA exhibited a mean diameter of ~150 nm (Fig. 1A). The variation in the mean diameter during the low-NO_x irradiation period was roughly 3%, *i.e.*, 145 nm. This variation was negligible and should not have influenced the extraction efficiency. Furthermore, Pospisilova *et al.*[30] observed a similar trend, *i.e.*, a larger decrease in the EESI signal compared to the SOA mass loading. In their experiment, the mean diameter of the SOA did not vary significantly under irradiation, which was consistent with our observations. Hence, the EESI signal decrease was most likely not caused by the EESI sensitivity dependence on the particles' diameter. Instead, Pospisilova *et al.*[30] proposed that the EESI-TOF was less sensitive to the composition of the aged α-pinene SOA, which were composed of a higher fraction of highly oxygenated compounds after irradiation. Lopez-Hilfiker *et al.*,[81] who characterized the EESI-TOF, showed that the instrument was the most sensitive for species with a relatively low oxygen number (O = 3–4 for carboxylic acids, 5–6 for saccharides and 4–6 for α-pinene SOA), while more oxygenated species were detected less efficiently. Bell *et al.*[93] also found that the EESI-TOF had a positive bias towards the less oxygenated monomers, and a negative bias towards highly oxygenated monomers and dimers. A possible explanation is that more oxygenated species are less volatile, which makes them less likely to evaporate and be measured by the instrument. On the other hand, less oxygenated species could more readily evaporate from the EESI droplets. Therefore, the formation of more oxygenated species at the expense of lower oxygen-containing monomers could explain the loss of EESI-TOF sensitivity. In contrast to the photodegradation period, the decay rates of the mass and EESI signal during the dark aging period were consistent, both decreasing by ~10% by the end of the low-NO_x experiment and by ~18% by the end of the high-NO_x experiment (Fig. S4†). Dark aging did not change the chemistry of the SOA enough to cause a change in the EESI sensitivity, underlying the importance of photochemical aging.

Photolysis rates of bulk SOA

During the low-NO_x experiment, photolysis rates of the total wall loss-corrected particle mass and the total EESI signal were estimated to be 3.5×10^{-3} s^{-1} and 2.7×10^{-3} s^{-1}, respectively. These photolysis rates were obtained using the method presented by Pospisilova *et al.*[30] In that previous study, photolysis rates of 6.5–7.6 $\times$ 10^{-4} s^{-1} for the particle mass and 4.1–5.6 $\times$ 10^{-4} s^{-1} for the EESI total signal were estimated. The differences in photolysis rates are likely caused by the fact that α-pinene-derived SOA are more photorecalcitrant than naphthalene-derived SOA. This is further supported by Romonosky *et al.*[94] who showed that naphthalene-derived SOA were more likely to be lost through photodegradation than α-pinene-derived SOA. Additionally, naphthalene-derived SOA in our low-NO_x experiment were formed under higher RH than Pospisilova *et al.*[30] Hence, naphthalene-derived SOA photolytic losses were most likely enhanced by the higher RH, as shown by Wong *et al.*[44] Indeed, photodissociation products in less viscous SOA (high RH) could more efficiently diffuse out of the particle, while recombination could have more time to happen in more viscous particles (low RH).

Global impact of photodegradation on SOA chemical composition

The time evolution of SOA species is depicted in Fig. 2A and B while the evolution of gaseous species is presented in Fig. 2C and D (t = 0 hours indicates when UV lights were turned on).

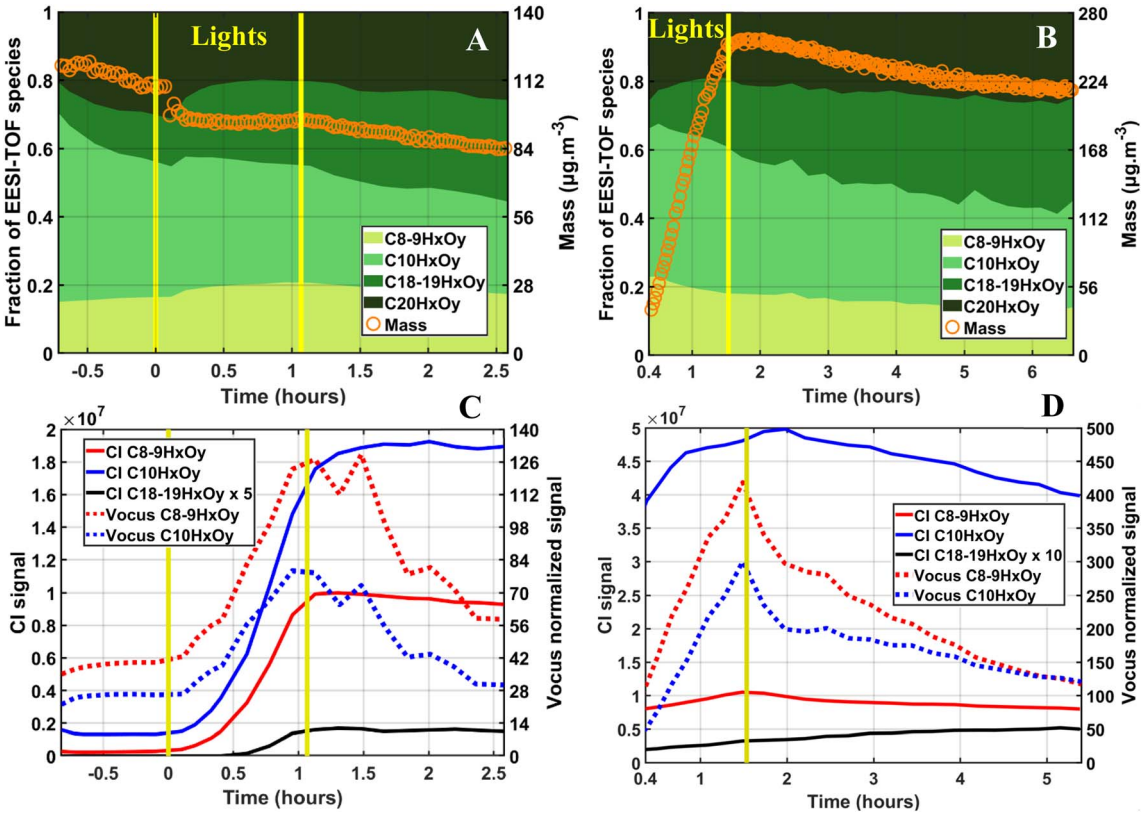

Fig. 2 Time evolution of the relative intensity of species (the sum of all compounds amounting to 1) and wall-corrected organic mass measured by the EESI-TOF and SMPS, respectively, for (A) the low-NO_x experiment ($t = -0.7$ hours to 2.6 hours) and (B) the high-NO_x experiment ($t = 0.4$ hours to 6.6 hours). The evolution of the signal for the gaseous species, measured by the CI (full lines) and the Vocus (dotted lines), was shown in (C) and (D) for the low-NO_x and high-NO_x experiments, respectively. The irradiation period started at $t = 0$ hours and is delimited by the yellow lines, ending just over $t = 1$ hour for (A) and (C), and ending at t ~1.5 hours for (C) and (D).

The time scale during the low-NO_x experiment showed species formed in the dark (Fig. 2A and C starting at $t = -0.7$ hours) before they were exposed to UV lights ($t = 0$ hours). During the high-NO_x experiment, the time scale of the experiment started after irradiation began (Fig. 2B and D starting at $t = 0.4$ hours), as species could not be detected by the EESI-TOF before that point. EESI-TOF figures (Fig. 2A and B) show the evolution of the relative intensity of the species, with all compounds combined amounting to 1. Gas-phase figures (Fig. 2C and D) show the evolution of the signals of compounds measured by the CI-Orbitrap and the Vocus. The compounds were grouped as $C_{8-9}H_xO_y$, $C_{10}H_xO_y$, $C_{18-19}H_xO_y$, and $C_{20}H_xO_y$, the first two groups being monomers and the last two groups being dimers. These compounds are expected to contain functionalities such as a peroxide group or an ester group as the linking functionality between the two monomeric units.[18,95] Dimeric compounds such as ester accretion products can also be produced from particulate-phase reactions.[95,96] Unfortunately, the instruments used in this study do not provide information about the chemical structures.

Fig. 2A shows that photodegradation-induced SOA mass loss correlated with a change in particle composition during the low-NO_x experiment. This change was seen for dimeric species, which evolved differently under irradiation depending on their carbon numbers. The main dimers produced from gas-phase chemistry, *i.e.*, $C_{20}H_xO_y$ species, experienced a net loss during photodegradation. On the other hand, the fraction of dimeric compounds with lower carbon numbers, *i.e.*, $C_{18-19}H_xO_y$ species, increased when the lights were on. The difference in dimer composition ($C_{20} \rightarrow C_{18,19}$) suggest that dimer photodegradation altered specifically $C_{20}H_xO_y$ species. Similar results were observed in Fig. 2B for the high-NO_x experiment. It should be noted that Lee *et al.*[91] showed a decrease in the double bond equivalent (DBE) which they associated with the fragmentation of larger naphthalene-derived SOA compounds.

Regarding the monomers during the low-NO_x experiment, the main species ($C_{10}H_xO_y$) initially increased when the lights were turned on and then slowly decreased under irradiation, while the $C_{8-9}H_xO_y$ molecules steadily increased with irradiation. It is worth mentioning that the fraction of monomers and dimers remained at similar levels (55% and 45% respectively) before and after the lights were on. This indicates that accretion reactions were not the main reaction pathway. The gaseous monomers and dimers species also increased, as seen in Fig. 2C. Comparing the evolution of gaseous C_{20} dimers was not possible since the instruments were not able to detect $C_{20}H_xO_y$. A possible reason is the prompt formation of new particles which reached high mass loadings and provided an additional

condensation sink that could have favored the partitioning of species with low volatility, such as $C_{20}H_xO_y$ oxidation products. However, the evolution of the gaseous monomers did not show significant differences between $C_{8-9}H_xO_y$ and $C_{10}H_xO_y$ where the gas-phase species were delayed for those formed in the particulate phase.

Finally, dimeric species also behaved differently than monomers in the dark. In the dark, both experiments showed that the fraction of particulate $C_{10}H_xO_y$ and $C_{8-9}H_xO_y$ started decreasing once irradiation stopped, while the fraction of dimers increased. This process was probably not linked to partitioning, as the gas-phase monomers remained stable or decreased in the dark. Species detected by the Vocus seemed to decrease faster than those measured by the CI-Orbitrap, most likely due to the instrument's selectivity toward different species.[74,80]

Photodegradation of C_xH_y compounds

To elucidate which compounds were optically active or formed from the photodegradation, oxidation products were sorted out according to their carbon and hydrogen numbers as well as their evolution. Before photodegradation in the low-NO_x experiment, $C_{20}H_{16-22}O_y$ had high relative signals (see Fig. 3 or Table S3† for numeric values). As shown in Fig. S2,† such compounds can be expected from bimolecular RO_2 reactions and can rapidly condense and partition to the particle-phase due to their low vapor pressure. However, these species could also have been formed from particle-phase reactions. The current data does not allow to confirm the dominance of one pathway to another. Nevertheless, these species increased in the dark before being depleted by the photodegradation process which led to the production of species with a different number of carbon, hydrogen, and oxygen atoms.

During the low-NO_x experiment, photodegradation was not uniform across all dimeric compounds and appeared to be dependent on the hydrogen number. The most saturated C_{20} species (*i.e.*, $C_{20}H_{18-22}O_y$), which were expected from radical reactions as described before, experienced a greater loss under irradiation than the compounds having larger DBE (*e.g.*, $C_{20}H_{14,16}O_y$). Similarly, the increase of relative signal for C_{18-19} species was more important for the most unsaturated species (*e.g.*, $C_{18-19}H_{14-16}O_y$) than for the ones with a higher hydrogen-content. This indicated that the unsaturated species were mainly produced when the UV lights were on. It is worth noting that they were moderately formed from gas-phase chemistry and then remained constant in the condensed phase when the UV lights were off.

This difference in reactivity could also be explained by the nature of the functional groups present in the molecule. It is known that carbonyl and peroxy moieties are photolabile and likely to be depleted under irradiation.[97] It has also been shown that photodegradation results in an increase of species carrying a carboxylic acid group.[30,65,97] Replacing an organic peroxy functional group with a carboxylic acid would be associated with the loss of at least 2 hydrogen atoms, which aligns with the increase of unsaturated dimers. Additionally, dimers with a high H number probably did not bear functional groups associated with a reduced H content, such as carbonyls and carboxylic acids. Instead, they were more likely to bear organic peroxide moieties or hydroxyl groups. Finally, similar observations can be made for monomeric species such as $C_{10}H_xO_y$, decreasing under the UV

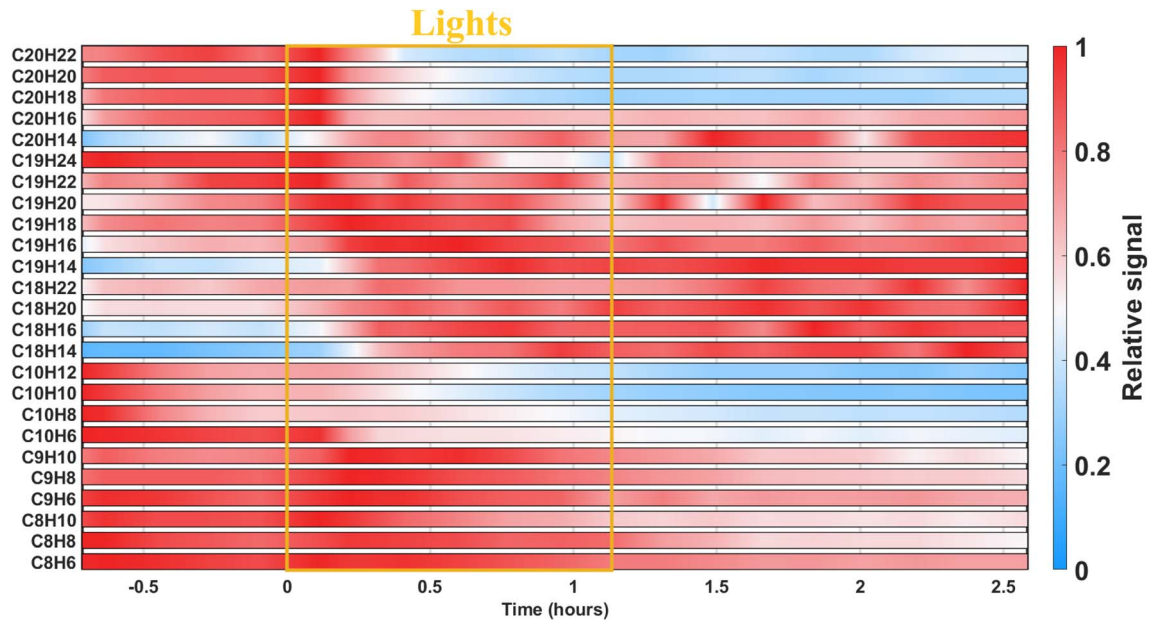

Fig. 3 Evolution of the relative signal of particle-phase species during the low-NO_x experiment, with compounds grouped by carbon and hydrogen numbers. Red indicates that the species are close to their maximum relative intensity, while blue signals a low relative intensity. UV lights are indicated by the yellow box.

lights due to photodegradation, with the most saturated species (*i.e.*, $C_{10}H_{10-12}O_y$) decreasing more than the ones with lower H content ($C_{10}H_{6-8}O_y$). $C_8H_xO_y$ behaved similarly, although the variations were not as important as for $C_{10}H_xO_y$. Interestingly, these changes appeared to be exclusive to the particulate phase, as all gas-phase monomers increased homogeneously under irradiation as depicted in Fig. S6.† Similar results were found in the high-NO_x experiment, as shown in Fig. S7,† for both non-N-containing and N-containing dimers. This suggests that autoxidation reactions resulted in oxidation products bearing photolabile functional groups (such as carbonyls)[40,42–44] under both low- and high-NO_x levels.

Evolution of individual species under irradiation

After having determined how the families of species evolved under UV lights, variations of the individual particulate monomers and dimers during the low-NO_x experiment were

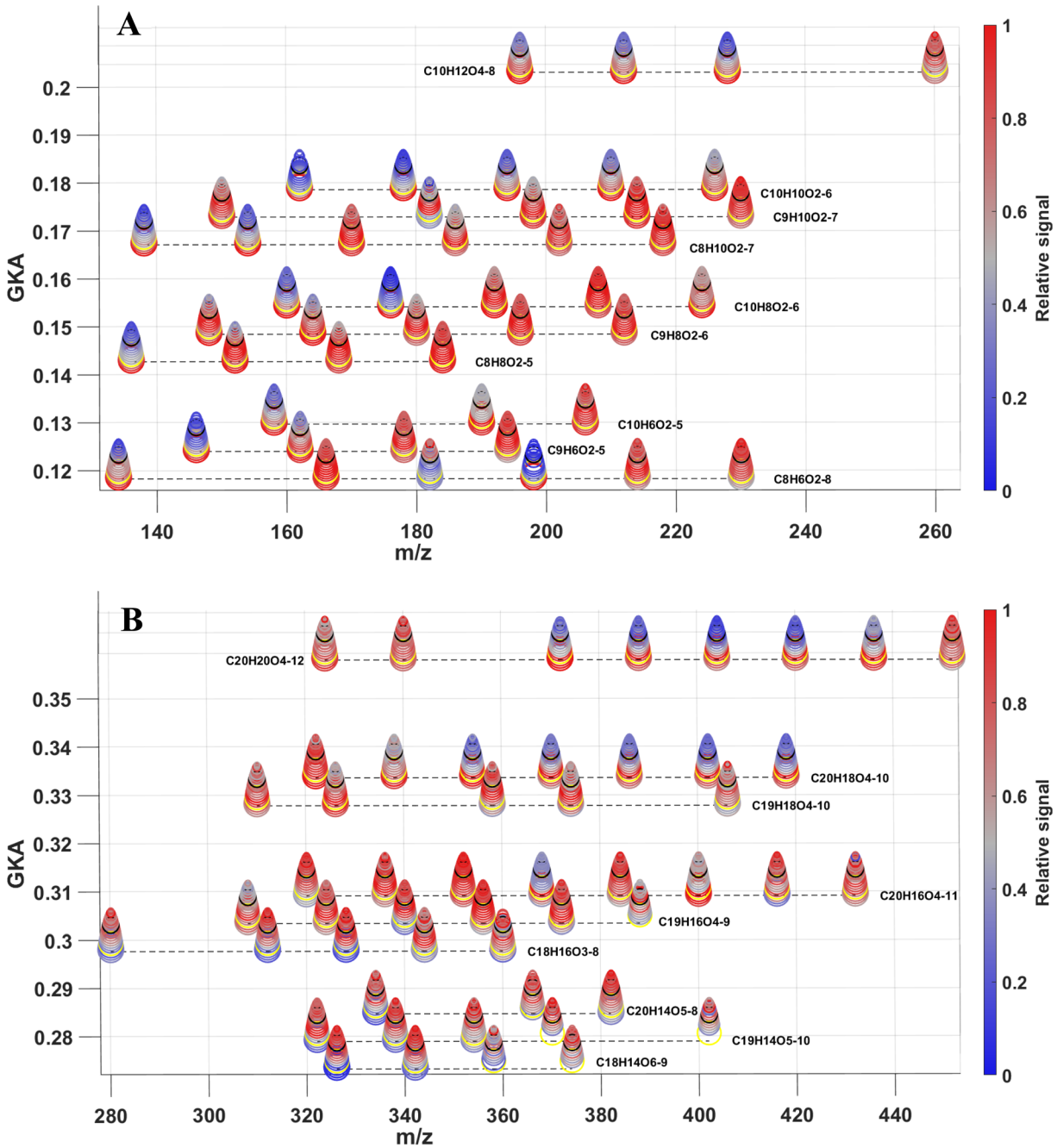

Fig. 4 Stacked generalized Kendrick analysis plots for (A) monomers and (B) dimers during the low-NO_x experiment. The multiple rings show the elapsed time from the start of the experiment (largest and lowest ring) to the end of the experiment (smallest and highest ring). The relative intensity of each compound is indicated by the color (blue = low intensity, red = high intensity, grey = medium intensity). The yellow and black rings indicate the beginning and the end of the irradiation period respectively.

further explored as shown in Fig. 4A and B respectively. This was done using stacked general Kendrick analysis (GKA) plots. GKA plots are related to traditional Kendrick mass defect analysis but use a tunable parameter to contract or expand the mass scale and a base unit that determines the horizontal alignment of the species. In this study, the base unit chosen was oxygen, so species were plotted horizontally according to their oxygen content. To generate the stacked figures, GKA values were calculated for different experimental times using the method presented by Alton *et al.*,[98] and were then stacked on top of each other to represent the time evolution of the relative intensity of the compounds. Many low-oxygenated species (O = 2–4), both for $C_{8-9}H_xO_y$ and $C_{10}H_xO_y$, decreased under irradiation. This suggests that photolabile functional groups were already present even for low-oxygenated species. Therefore, the OH-initiated oxidation of naphthalene must have resulted in at least one photolabile moiety early on. This was supported by previous studies showing monomers with a low oxygen content bearing carbonyl functional groups.[84,85,99] However, it cannot be ruled out that the loss of $C_{8-10}H_xO_{2-4}$ could also be due to repartitioning from the particle-phase to the gas-phase, as proposed by Pospisilova *et al.*[30] As a result, the less oxygenated particulate monomers were then possibly depleted both by photodegradation and/or evaporation. More oxidized species should also have been sensitive to photodegradation but seemed to increase (*e.g.*, $C_8H_8O_{3-5}$, $C_9H_6O_{4-5}$, $C_9H_8O_{4-6}$, and $C_9H_{10}O_{5-7}$) or remain stable during irradiation, as also observed in previous studies.[30,97] The lack of loss could be explained by the presence of photorecalcitrant functional groups such as carboxylic acids or through the production of oxidants in the particle-phase during irradiation producing highly oxygenated monomers.[26] Another source of those species would be gas-phase compounds condensing after being formed under UV lights (Fig. S8-B†). The decay in the dark of the compounds within one family seemed to also depend slightly on the O content of the species, as the most oxidized particulate compounds decayed more slowly (*e.g.*, $C_9H_{10}O_7$ compared to $C_9H_{10}O_2$). Higher oxygenated compounds have lower volatility, meaning that even with photodegradation they could continue to have sufficiently low volatility to remain in the particle-phase.

The evolution of the dimers is presented in Fig. 4B. Similarly to the monomers, the photodegradation efficiency of the $C_{20}H_{16-20}O_y$ compounds was dependent on the oxygen number. However, whereas many low-oxygenated monomers were lost upon photodegradation, this was not the case for the dimers, the low-oxidized dimers seeming less inclined to be photodegraded. Contrariwise to the monomers, dimers with a low oxygen content (O = 3–5) were less likely to evaporate from the particle phase. Additionally, $C_{20}H_xO_y$ species with a low number of oxygen atoms were less photodegraded. A possible explanation is that less oxygenated $C_{20}H_xO_y$ species possessed fewer functional groups, which decreased the chance of carrying a photolabile functional group. Furthermore, low-oxygenated dimers could also have been formed from the photodegradation of the more oxygenated dimers. Almost all the $C_{18-19}H_{14-18}O_y$ showed an increase in production during irradiation. The clearest increase concerned $C_{18-19}H_{14-16}O_{\leq 7}$ species, *i.e.*, unsaturated low-oxidized dimers. This was consistent with the results of the $C_{20}H_{16-20}O_y$, whose photodegradation would have resulted in $C_{18-19}H_xO_y$. Many of the $C_{18-19}H_{14-16}O_{>7}$ compounds were not present at first, but were formed during irradiation. Overall, this showed that the photodegradation of the particles was not only dependent on the hydrogen and carbon numbers but also on the oxygen number of a molecule. The global O : C ratio slightly increased after the photodegradation (from 0.408 to 0.417), which was similar to the observations in Bateman *et al.*,[97] who showed an increased O : C ratio after the irradiation of D-limonene-derived SOA. Results from high- and low-NO_x experiments were consistent as presented in Fig. S10.†

Emission of volatile species from particle- to gas-phase following photodegradation

The photodegradation of $C_{20}H_{16-20}O_y$ to $C_{18-19}H_{14-16}O_y$ would most likely result in the emission of formic acid (HC(O)OH), formaldehyde (HCHO), acetic acid ($CH_3C(O)OH$), or acetaldehyde (CH_3CHO) to the gas-phase, as proposed in Fig. 5A. The emission of these species is a distinctive sign of photodegradation that has been shown in multiple SOA photodegradation studies.[35–37,44,97] We investigated the production of these species using the Vocus and found that formic acid, acetic acid, and acetaldehyde increased during photodegradation (Fig. 5B and C). This confirms the photodegradation pathway and has important atmospheric implications. Indeed, these species are also highly important in the atmosphere due to their abundance, the acids' ability to contribute to the free atmospheric acidity, and the aldehydes' role as transition species leading to the formation of HO_2 or CO in the atmosphere.[100,101]

To estimate the concentrations of acetic acid, formic acid, and acetaldehyde emitted, previous experiments from the same campaign using known amounts of monoterpene injected as well as the Vocus sensitivity towards these monoterpenes were used. Furthermore, we estimated the sensitivity of the Vocus towards the photodegradation volatile species by comparing the differences in instrumental sensitivity between monoterpene and organic acids/carbonyls from another study.[102] The resulting concentrations are shown in Table 1 and reached in the low-NO_x experiment up to 3 ppb, 0.5 ppb, and 0.07 ppb of acetic acid, formic acid, and acetaldehyde, respectively. During the high-NO_x experiment, emissions reached up to 10 ppb, 1 ppb, and 0.08 ppb for acetic acid, formic acid, and acetaldehyde, respectively. The amounts of volatile products emitted were consistent with the loss of SOA mass in the low-NO_x experiment, but it should be noted that these results remain qualitative.

Evolution of the volatility pre-to post-photodegradation

To characterize the change in the particles' physical properties that is expected from the changed chemical composition, the effective saturation mass concentration (C^*) of each particulate oxidation product has been calculated. The estimation was made using the equation from Li *et al.*[103] and followed their structural and formulaic estimations. Particle-phase oxidation products were categorized as intermediate volatile organic compounds (IVOCs), semi-volatile organic compounds (SVOCs),

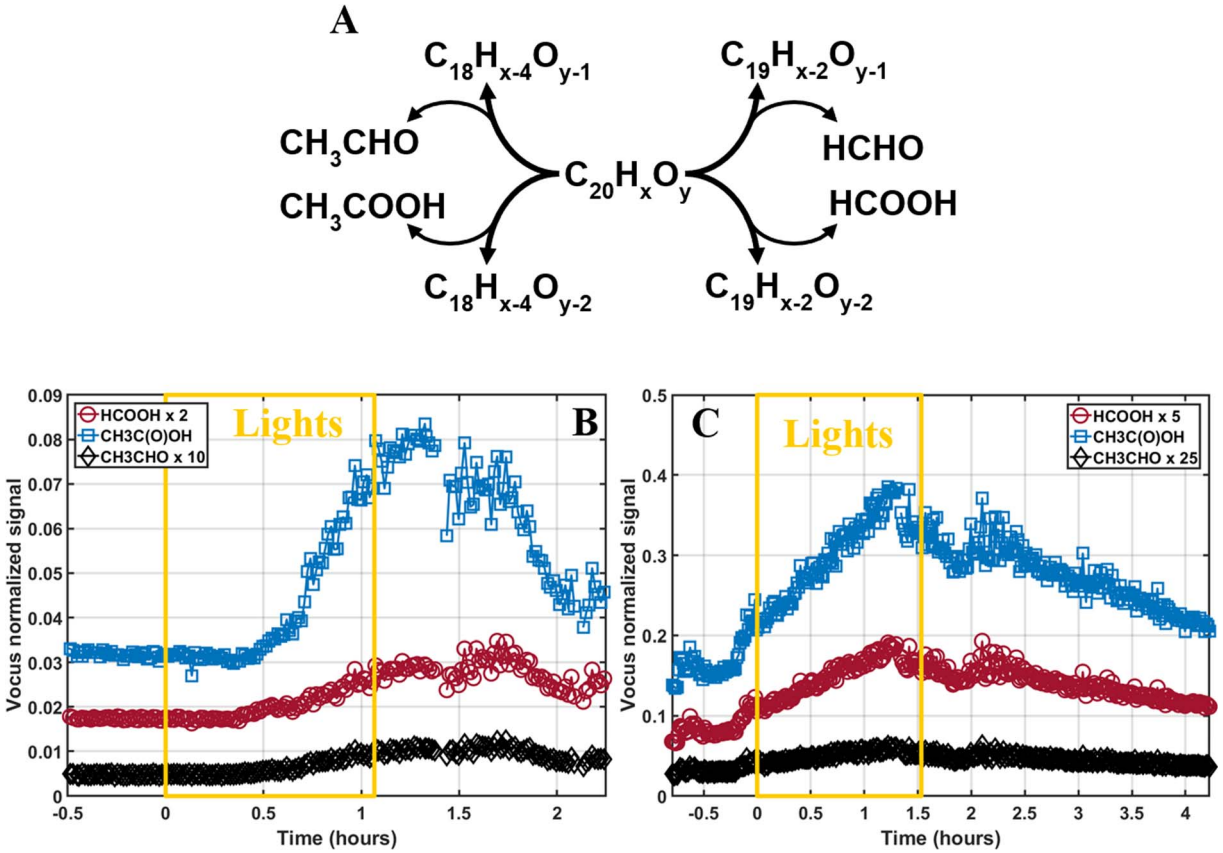

Fig. 5 (A) Photodegradation mechanism of $C_{20}H_xO_y$ dimers. The time evolution of formic acid (HC(O)OH), acetic acid ($CH_3C(O)OH$), and acetaldehyde (CH_3CHO) are shown during (B) low- and (C) high-NO_x experiments. The intensity of the HC(O)OH and CH_3CHO signals was adjusted for easier visualization. $t = 0$ hours indicate the start of lights, and the yellow box indicates the irradiation period.

Table 1 Maximum estimated amounts of volatile species emitted during photodegradation during the low- and high-NO_x experiments. To estimate these amounts, the normalized signals to injected masses ratios of monoterpene were used (corrected for the instrument sensitivity)

	ppb	μg m^{-3}	SOA mass loss	% Of SOA loss from the volatile species
Low-NO_x	Acetic acid: 3 Formic acid: 0.5 Acetaldehyde: 0.07	Acetic acid: 7.5 Formic acid: 0.93 Acetaldehyde: 0.12	14 μg m^{-3}	Acetic acid: 54% Formic acid: 7% Acetaldehyde: 0.9%
High-NO_x	Acetic acid: 10 Formic acid: 1 Acetaldehyde: 0.08	Acetic acid: 25 Formic acid: 2.3 Acetaldehyde: 0.15	✗	✗

low volatile organic compounds (LVOCs), extremely low volatile organic compounds (ELVOCs), and ultra-low volatile organic compounds (ULVOCs) according to their estimated C^*. Fig. 6 shows how the fraction of these species evolved during the low-NO_x experiment pre- (Fig. 6A) to post-photodegradation (Fig. 6B). The fraction of the species during the high-NO_x experiment at the beginning of the photodegradation and after photodegradation ended are displayed in Fig. 6C and D, respectively. Both experiments showed that species with low volatilities (*i.e.* LVOCs, ELVOCs and ULVOCs) slightly increased in both experiments after the particles were photodegraded. Additionally, the mean C^* was calculated and showed that irradiated particles were less volatile after photodegradation (from 0.74 to 0.67 μg m^{-3} for low-NO_x and from 1.53 to 1.04 μg m^{-3} for high-NO_x). Low-NO_x particles globally showed a lower C^* than high-NO_x particles, but low-NO_x C^* also did not decrease as much as high-NO_x C^* after irradiation. This was consistent with the larger decrease of IVOC post-photodegradation for the high-NO_x experiment. Although C^* variations were not very significant, they still agreed with the results from Pospisilova *et al.*[30] who showed that α-pinene SOA presented lower volatility after its exposure to UV lights by performing isothermal evaporation experiments. However, our results may have been influenced by changes in the parametrizations used to calculate C^*. Indeed, these parametrizations may have differed from pre-photodegradation to post-

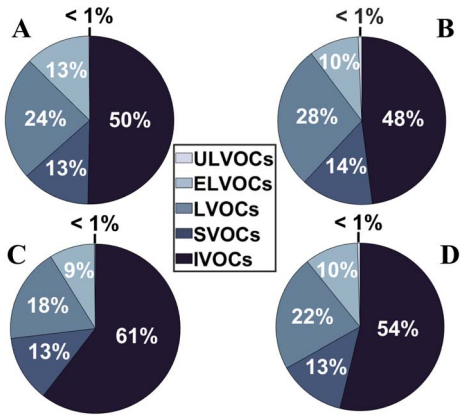

Fig. 6 (A) Volatility distribution of the particulate oxidation products for the low-NO_x experiment before photodegradation ($t = -0.1$ h) and (B) after photodegradation ($t = 1.13$ h). (C) Volatility distribution for the high-NO_x experiment at the beginning of photodegradation ($t = 0.37$ h) and (D) after photodegradation ($t = 1.73$ h). Colors indicate the fraction of ultra-low volatilite (ULVOCs), extremely low volatilite (ELVOCs), low volatilite (LVOCs), semi-volatile (SVOCs) and intermediate volatilite (IVOCs) organic compounds respectively.

photodegradation as the functional groups in the particle-phase compounds could have changed. The fraction of non-N-containing and N-containing species in the high-NO_x experiment remained unaffected by photodegradation. It went from a 0.76/0.24 ratio for non-N-containing and N-containing species respectively at the beginning of photodegradation ($t = 0.4$ hours) to a 0.75/0.25 ratio after photodegradation ($t = 1.7$ hours).

Conclusion

This study investigated the composition of naphthalene SOA and the influence of photodegradation as a marker for anthropogenic VOC/PAH aerosol photodegradation due to its abundance and role in urban environments. Our results showed that the changes observed in particles aging under irradiation were significantly greater than the variations caused by other chemical processes. These other processes were controlled by letting particles age under a similar timescale in the dark. Prominent degradation (2/3 loss) of the C_{20} dimers during photodegradation was revealed through an in-depth molecular characterization of naphthalene-derived SOA. The degradation of the dimers yielded particulate-phase fragmentation products with C_{18-19} while releasing C_{1-2} gaseous compounds. Photodegradation was found to be dependent on the chemical composition and functional groups with hydroperoxide and carbonyl species being the most photolabile groups. SOA physical properties were also affected by photodegradation, as particles showed a decrease in volatility. Further work coupling the EESI-TOF to a thermal denuder as done by Bell *et al.*[93] would provide more accurate information about the particles changing volatilities.

The photochemical process was accompanied by a loss of particle mass under irradiation (−12%) which corresponded to the release of volatile products. Among them, three products playing a major role in global atmospheric chemistry were identified: formic acid, acetic acid, and acetaldehyde. These results highlight the need to consider photochemical activity as one of the main drivers of SOA aging as naphthalene-derived SOA and other anthropogenic-sourced aerosols are an important factor affecting health, visibility, and the environment. Predicting their impact on any of these subjects requires information about their chemical composition and physical properties, both of which are modified due to UV irradiation, showcasing the complexity of considering SOA photodegradation in broader atmospheric issues.

Data availability

The data that support the findings of this study are available on request from the corresponding authors, D. B. at: david.bell@psi.ch and/or M. R. at: matthieu.riva@ircelyon.univ-lyon1.fr.

Conflicts of interest

There are no conflicts to declare.

Acknowledgements

We thank the European Research Council (ERC-StG MAARvEL; no. 852161), the European Union's Horizon 2020 research and innovation program through the ATMO-ACCESS Integrating Activity under grant agreement no. 101008004, as well the Swiss National Foundation (SNF – grant no. 200021 213071) for their financial support. PSI's atmospheric simulation chamber is a facility of ACTRIS ERIC and receives funding from the Swiss State Secretariat for Education, Research and Innovation (SERI). We thank as well the Orbitool team for developing the tools to analyze Orbitrap mass spectra data.

References

1 R. Burnett, H. Chen, M. Szyszkowicz, N. Fann, B. Hubbell, C. A. Pope, J. S. Apte, M. Brauer, A. Cohen, S. Weichenthal, J. Coggins, Q. Di, B. Brunekreef, J. Frostad, S. S. Lim, H. Kan, K. D. Walker, G. D. Thurston, R. B. Hayes, C. C. Lim, M. C. Turner, M. Jerrett, D. Krewski, S. M. Gapstur, W. R. Diver, B. Ostro, D. Goldberg, D. L. Crouse, R. V. Martin, P. Peters, L. Pinault, M. Tjepkema, A. Van Donkelaar, P. J. Villeneuve, A. B. Miller, P. Yin, M. Zhou, L. Wang, N. A. H. Janssen, M. Marra, R. W. Atkinson, H. Tsang, T. Quoc Thach, J. B. Cannon, R. T. Allen, J. E. Hart, F. Laden, G. Cesaroni, F. Forastiere, G. Weinmayr, A. Jaensch, G. Nagel, H. Concin and J. V. Spadaro, Global estimates of mortality associated with long-term exposure to outdoor fine particulate matter, *Proc. Natl. Acad. Sci. U. S. A.*, 2018, **115**, 9592–9597.

2 M. Shiraiwa, K. Ueda, A. Pozzer, G. Lammel, C. J. Kampf, A. Fushimi, S. Enami, A. M. Arangio, J. Fröhlich-Nowoisky,

Y. Fujitani, A. Furuyama, P. S. J. Lakey, J. Lelieveld, K. Lucas, Y. Morino, U. Pöschl, S. Takahama, A. Takami, H. Tong, B. Weber, A. Yoshino and K. Sato, Aerosol Health Effects from Molecular to Global Scales, *Environ. Sci. Technol.*, 2017, **51**, 13545–13567.

3 T. Déméautis, M. Delles, S. Tomaz, G. Monneret, O. Glehen, G. Devouassoux, C. George and A. Bentaher, Pathogenic Mechanisms of Secondary Organic Aerosols, *Chem. Res. Toxicol.*, 2022, **35**(7), 1146–1161.

4 U. Pöschl, Atmospheric Aerosols: Composition, Transformation, Climate and Health Effects, *Angew. Chem., Int. Ed.*, 2005, **44**, 7520–7540.

5 J. Haywood and O. Boucher, Estimates of the direct and indirect radiative forcing due to tropospheric aerosols: A review, *Rev. Geophys.*, 2000, **38**, 513–543.

6 *Clouds in the Perturbed Climate System: Their Relationship to Energy Balance, Atmospheric Dynamics, and Precipitation*, ed. J. Heintzenberg and R. J. Charlson, MIT Press, Cambridge, Mass, 2009.

7 U. Lohmann and J. Feichter, Global indirect aerosol effects: a review, *Atmos. Chem. Phys.*, 2005, **5**(3), 715–737.

8 S. Twomey, The nuclei of natural cloud formation part II: The supersaturation in natural clouds and the variation of cloud droplet concentration, *Geofis. Pura Appl.*, 1959, **43**, 243–249.

9 B. A. Albrecht, Aerosols, Cloud Microphysics, and Fractional Cloudiness, *Science*, 1989, **245**, 1227–1230.

10 R. Pincus and M. B. Baker, Effect of precipitation on the albedo susceptibility of clouds in the marine boundary layer, *Nature*, 1994, **372**, 250–252.

11 M. Kanakidou, J. H. Seinfeld, S. N. Pandis, I. Barnes, F. J. Dentener, M. C. Facchini, R. V. Dingenen, B. Ervens, A. Nenes, C. J. Nielsen, E. Swietlicki, J. P. Putaud, Y. Balkanski, S. Fuzzi, J. Horth, G. K. Moortgat, R. Winterhalter, C. E. L. Myhre, K. Tsigaridis, E. Vignati, E. G. Stephanou and J. Wilson, Organic aerosol and global climate modelling: a review, *Atmos. Chem. Phys.*, 2005, **5**(4), 1053–1123.

12 J. L. Jimenez, M. R. Canagaratna, N. M. Donahue, A. S. H. Prevot, Q. Zhang, J. H. Kroll, P. F. DeCarlo, J. D. Allan, H. Coe, N. L. Ng, A. C. Aiken, K. S. Docherty, I. M. Ulbrich, A. P. Grieshop, A. L. Robinson, J. Duplissy, J. D. Smith, K. R. Wilson, V. A. Lanz, C. Hueglin, Y. L. Sun, J. Tian, A. Laaksonen, T. Raatikainen, J. Rautiainen, P. Vaattovaara, M. Ehn, M. Kulmala, J. M. Tomlinson, D. R. Collins, M. J. Cubison, E. J. Dunlea, J. A. Huffman, T. B. Onasch, M. R. Alfarra, P. I. Williams, K. Bower, Y. Kondo, J. Schneider, F. Drewnick, S. Borrmann, S. Weimer, K. Demerjian, D. Salcedo, L. Cottrell, R. Griffin, A. Takami, T. Miyoshi, S. Hatakeyama, A. Shimono, J. Y. Sun, Y. M. Zhang, K. Dzepina, J. R. Kimmel, D. Sueper, J. T. Jayne, S. C. Herndon, A. M. Trimborn, L. R. Williams, E. C. Wood, A. M. Middlebrook, C. E. Kolb, U. Baltensperger and D. R. Worsnop, Evolution of Organic Aerosols in the Atmosphere, *Science*, 2009, **326**, 1525–1529.

13 J. G. Watson, J. C. Chow and E. M. Fujita, Review of volatile organic compound source apportionment by chemical mass balance, *Atmos. Environ.*, 2001, **35**, 1567–1584.

14 A. Kansal, Sources and reactivity of NMHCs and VOCs in the atmosphere: A review, *J. Hazard. Mater.*, 2009, **166**, 17–26.

15 A. Guenther, C. N. Hewitt, D. Erickson, R. Fall, C. Geron, T. Graedel, P. Harley, L. Klinger, M. Lerdau, W. A. Mckay, T. Pierce, B. Scholes, R. Steinbrecher, R. Tallamraju, J. Taylor and P. Zimmerman, A global model of natural volatile organic compound emissions, *J. Geophys. Res.:Atmos.*, 1995, **100**, 8873–8892.

16 A. B. Guenther, X. Jiang, C. L. Heald, T. Sakulyanontvittaya, T. Duhl, L. K. Emmons and X. Wang, The Model of Emissions of Gases and Aerosols from Nature version 2.1 (MEGAN2.1): an extended and updated framework for modeling biogenic emissions, *Geosci. Model Dev.*, 2012, **5**, 1471–1492.

17 K. Sindelarova, C. Granier, I. Bouarar, A. Guenther, S. Tilmes, T. Stavrakou, J.-F. Müller, U. Kuhn, P. Stefani and W. Knorr, Global data set of biogenic VOC emissions calculated by the MEGAN model over the last 30 years, *Atmos. Chem. Phys.*, 2014, **14**, 9317–9341.

18 M. Hallquist, J. C. Wenger, U. Baltensperger, Y. Rudich, D. Simpson, M. Claeys, J. Dommen, N. M. Donahue, C. George, A. H. Goldstein, J. F. Hamilton, H. Herrmann, T. Hoffmann, Y. Iinuma, M. Jang, M. E. Jenkin, J. L. Jimenez, A. Kiendler-Scharr, W. Maenhaut, G. McFiggans, T. F. Mentel, A. Monod, A. S. H. Prevot, J. H. Seinfeld, J. D. Surratt, R. Szmigielski and J. Wildt, The formation, properties and impact of secondary organic aerosol: current and emerging issues, *Atmos. Chem. Phys.*, 2009, **9**(14), 5155–5236.

19 Y.-H. Lin, Z. Zhang, K. S. Docherty, H. Zhang, S. H. Budisulistiorini, C. L. Rubitschun, S. L. Shaw, E. M. Knipping, E. S. Edgerton, T. E. Kleindienst, A. Gold and J. D. Surratt, Isoprene Epoxydiols as Precursors to Secondary Organic Aerosol Formation: Acid-Catalyzed Reactive Uptake Studies with Authentic Compounds, *Environ. Sci. Technol.*, 2012, **46**, 250–258.

20 P. Mettke, M. Brüggemann, A. Mutzel, R. Gräfe and H. Herrmann, Secondary Organic Aerosol (SOA) through Uptake of Isoprene Hydroxy Hydroperoxides (ISOPOOH) and its Oxidation Products, *ACS Earth Space Chem.*, 2023, **7**, 1025–1037.

21 I. Riipinen, J. R. Pierce, T. Yli-Juuti, T. Nieminen, S. Häkkinen, M. Ehn, H. Junninen, K. Lehtipalo, T. Petäjä, J. Slowik, R. Chang, N. C. Shantz, J. Abbatt, W. R. Leaitch, V.-M. Kerminen, D. R. Worsnop, S. N. Pandis, N. M. Donahue and M. Kulmala, Organic condensation: a vital link connecting aerosol formation to cloud condensation nuclei (CCN) concentrations, *Atmos. Chem. Phys.*, 2011, **11**, 3865–3878.

22 X. Zhang, S. N. Pandis and J. H. Seinfeld, Diffusion-Limited Versus Quasi-Equilibrium Aerosol Growth, *Aerosol Sci. Technol.*, 2012, **46**, 874–885.

23 M. Ehn, J. A. Thornton, E. Kleist, M. Sipilä, H. Junninen, I. Pullinen, M. Springer, F. Rubach, R. Tillmann, B. Lee, F. Lopez-Hilfiker, S. Andres, I.-H. Acir, M. Rissanen, T. Jokinen, S. Schobesberger, J. Kangasluoma, J. Kontkanen, T. Nieminen, T. Kurtén, L. B. Nielsen, S. Jørgensen, H. G. Kjaergaard, M. Canagaratna, M. D. Maso, T. Berndt, T. Petäjä, A. Wahner, V.-M. Kerminen, M. Kulmala, D. R. Worsnop, J. Wildt and T. F. Mentel, A large source of low-volatility secondary organic aerosol, *Nature*, 2014, **506**, 476–479.

24 F. Bianchi, T. Kurtén, M. Riva, C. Mohr, M. P. Rissanen, P. Roldin, T. Berndt, J. D. Crounse, P. O. Wennberg, T. F. Mentel, J. Wildt, H. Junninen, T. Jokinen, M. Kulmala, D. R. Worsnop, J. A. Thornton, N. Donahue, H. G. Kjaergaard and M. Ehn, Highly Oxygenated Organic Molecules (HOM) from Gas-Phase Autoxidation Involving Peroxy Radicals: A Key Contributor to Atmospheric Aerosol, *Chem. Rev.*, 2019, **119**, 3472–3509.

25 C. George, M. Ammann, B. D'Anna, D. J. Donaldson and S. A. Nizkorodov, Heterogeneous Photochemistry in the Atmosphere, *Chem. Rev.*, 2015, **115**, 4218–4258.

26 L. Gerritz, J. Wei, T. Fang, C. Wong, A. L. Klodt, S. A. Nizkorodov and M. Shiraiwa, Reactive Oxygen Species Formation and Peroxide and Carbonyl Decomposition in Aqueous Photolysis of Secondary Organic Aerosols, *Environ. Sci. Technol.*, 2024, **58**, 4716–4726.

27 J. H. Kroll and J. H. Seinfeld, Chemistry of secondary organic aerosol: Formation and evolution of low-volatility organics in the atmosphere, *Atmos. Environ.*, 2008, **42**, 3593–3624.

28 A. Zare, K. M. Fahey, G. Sarwar, R. C. Cohen and H. O. T. Pye, Vapor-Pressure Pathways Initiate but Hydrolysis Products Dominate the Aerosol Estimated from Organic Nitrates, *ACS Earth Space Chem.*, 2019, **3**, 1426–1437.

29 H. J. Chacon-Madrid and N. M. Donahue, Fragmentation vs. functionalization: chemical aging and organic aerosol formation, *Atmos. Chem. Phys.*, 2011, **11**, 10553–10563.

30 V. Pospisilova, D. M. Bell, H. Lamkaddam, A. Bertrand, L. Wang, D. Bhattu, X. Zhou, J. Dommen, A. S. H. Prevot, U. Baltensperger, I. El Haddad and J. G. Slowik, Photodegradation of α-Pinene Secondary Organic Aerosol Dominated by Moderately Oxidized Molecules, *Environ. Sci. Technol.*, 2021, **55**, 6936–6943.

31 T. Tritscher, J. Dommen, P. F. DeCarlo, M. Gysel, P. B. Barmet, A. P. Praplan, E. Weingartner, A. S. H. Prévôt, I. Riipinen, N. M. Donahue and U. Baltensperger, Volatility and hygroscopicity of aging secondary organic aerosol in a smog chamber, *Atmos. Chem. Phys.*, 2011, **11**, 11477–11496.

32 T. Feng, Y. Wang, W. Hu, M. Zhu, W. Song, W. Chen, Y. Sang, Z. Fang, W. Deng, H. Fang, X. Yu, C. Wu, B. Yuan, S. Huang, M. Shao, X. Huang, L. He, Y. R. Lee, L. G. Huey, F. Canonaco, A. S. H. Prevot and X. Wang, Impact of aging on the sources, volatility, and viscosity of organic aerosols in Chinese outflows, *Atmos. Chem. Phys.*, 2023, **23**, 611–636.

33 Y. Zhang, M. Cheng, J. Gao and J. Li, Review of the influencing factors of secondary organic aerosol formation and aging mechanism based on photochemical smog chamber simulation methods, *J. Environ. Sci.*, 2023, **123**, 545–559.

34 M. L. Walser, J. Park, A. L. Gomez, A. R. Russell and S. A. Nizkorodov, Photochemical Aging of Secondary Organic Aerosol Particles Generated from the Oxidation of d-Limonene, *J. Phys. Chem. A*, 2007, **111**, 1907–1913.

35 S. A. Mang, D. K. Henricksen, A. P. Bateman, M. P. S. Andersen, D. R. Blake and S. A. Nizkorodov, Contribution of Carbonyl Photochemistry to Aging of Atmospheric Secondary Organic Aerosol, *J. Phys. Chem. A*, 2008, **112**, 8337–8344.

36 X. Pan and J. S. Underwood, Photodegradation of secondary organic aerosol generated from limonene oxidation by ozone studied with chemical ionization mass spectrometry, *Atmos. Chem. Phys.*, 2009, **9**(12), 3851–3865.

37 K. T. Malecha and S. A. Nizkorodov, Photodegradation of Secondary Organic Aerosol Particles as a Source of Small, Oxygenated Volatile Organic Compounds, *Environ. Sci. Technol.*, 2016, **50**, 9990–9997.

38 C. Wu, D. M. Bell, E. L. Graham, S. Haslett, I. Riipinen, U. Baltensperger, A. Bertrand, S. Giannoukos, J. Schoonbaert, I. El Haddad, A. S. H. Prevot, W. Huang and C. Mohr, Photolytically induced changes in composition and volatility of biogenic secondary organic aerosol from nitrate radical oxidation during night-to-day transition, *Atmos. Chem. Phys.*, 2021, **21**, 14907–14925.

39 J. E. Shilling, M. A. Zawadowicz, J. Liu, R. A. Zaveri and A. Zelenyuk, Photochemical Aging Alters Secondary Organic Aerosol Partitioning Behavior, *ACS Earth Space Chem.*, 2019, **3**, 2704–2716.

40 M. Krapf, I. El Haddad, E. A. Bruns, U. Molteni, K. R. Daellenbach, A. S. H. Prévôt, U. Baltensperger and J. Dommen, Labile Peroxides in Secondary Organic Aerosol, *Chem*, 2016, **1**, 603–616.

41 M. A. Zawadowicz, B. H. Lee, M. Shrivastava, A. Zelenyuk, R. A. Zaveri, C. Flynn, J. A. Thornton and J. E. Shilling, Photolysis Controls Atmospheric Budgets of Biogenic Secondary Organic Aerosol, *Environ. Sci. Technol.*, 2020, **54**, 3861–3870.

42 S. A. Epstein, S. L. Blair and S. A. Nizkorodov, Direct Photolysis of α-Pinene Ozonolysis Secondary Organic Aerosol: Effect on Particle Mass and Peroxide Content, *Environ. Sci. Technol.*, 2014, **48**, 11251–11258.

43 K. M. Henry and N. M. Donahue, Photochemical Aging of α-Pinene Secondary Organic Aerosol: Effects of OH Radical Sources and Photolysis, *J. Phys. Chem. A*, 2012, **116**, 5932–5940.

44 J. P. S. Wong, S. Zhou and J. P. D. Abbatt, Changes in Secondary Organic Aerosol Composition and Mass due to Photolysis: Relative Humidity Dependence, *J. Phys. Chem. A*, 2015, **119**, 4309–4316.

45 D. E. Romonosky, A. Laskin, J. Laskin and S. A. Nizkorodov, High-Resolution Mass Spectrometry and Molecular Characterization of Aqueous Photochemistry Products of Common Types of Secondary Organic Aerosols, *J. Phys. Chem. A*, 2015, **119**, 2594–2606.

46 K. S. Docherty, W. Wu, Y. B. Lim and P. J. Ziemann, Contributions of Organic Peroxides to Secondary Aerosol Formed from Reactions of Monoterpenes with O_3, *Environ. Sci. Technol.*, 2005, **39**, 4049–4059.

47 J. D. Surratt, S. M. Murphy, J. H. Kroll, N. L. Ng, L. Hildebrandt, A. Sorooshian, R. Szmigielski, R. Vermeylen, W. Maenhaut, M. Claeys, R. C. Flagan and J. H. Seinfeld, Chemical Composition of Secondary Organic Aerosol Formed from the Photooxidation of Isoprene, *J. Phys. Chem. A*, 2006, **110**, 9665–9690.

48 T. B. Nguyen, A. P. Bateman, D. L. Bones, S. A. Nizkorodov, J. Laskin and A. Laskin, High-resolution mass spectrometry analysis of secondary organic aerosol generated by ozonolysis of isoprene, *Atmos. Environ.*, 2010, **44**, 1032–1042.

49 P. Mertes, L. Pfaffenberger, J. Dommen, M. Kalberer and U. Baltensperger, Development of a sensitive long path absorption photometer to quantify peroxides in aerosol particles (Peroxide-LOPAP), *Atmos. Meas. Tech.*, 2012, **5**, 2339–2348.

50 S. Aimanant and P. J. Ziemann, Development of Spectrophotometric Methods for the Analysis of Functional Groups in Oxidized Organic Aerosol, *Aerosol Sci. Technol.*, 2013, **47**, 581–591.

51 K. M. Shakya and R. J. Griffin, Secondary Organic Aerosol from Photooxidation of Polycyclic Aromatic Hydrocarbons, *Environ. Sci. Technol.*, 2010, **44**, 8134–8139.

52 A. W. H. Chan, K. E. Kautzman, P. S. Chhabra, J. D. Surratt, M. N. Chan, J. D. Crounse, P. O. Wennberg, R. C. Flagan and J. H. Seinfeld, Secondary organic aerosol formation from photooxidation of naphthalene and alkylnaphthalenes: implications for oxidation of intermediate volatility organic compounds (IVOCs), *Atmos. Chem. Phys.*, 2009, **9**(9), 3049–3060.

53 H. O. T. Pye and G. A. Pouliot, Modeling the Role of Alkanes, Polycyclic Aromatic Hydrocarbons, and Their Oligomers in Secondary Organic Aerosol Formation, *Environ. Sci. Technol.*, 2012, **46**, 6041–6047.

54 D. S. Tkacik, A. A. Presto, N. M. Donahue and A. L. Robinson, Secondary Organic Aerosol Formation from Intermediate-Volatility Organic Compounds: Cyclic, Linear, and Branched Alkanes, *Environ. Sci. Technol.*, 2012, **46**, 8773–8781.

55 M. Tsapakis and E. G. Stephanou, Diurnal Cycle of PAHs, Nitro-PAHs, and oxy-PAHs in a High Oxidation Capacity Marine Background Atmosphere, *Environ. Sci. Technol.*, 2007, **41**, 8011–8017.

56 L. Wang and L. Wang, Atmospheric oxidation mechanism of acenaphthene initiated by OH radicals, *Atmos. Environ.*, 2020, **243**, 117870.

57 M. Riva, R. M. Healy, P.-M. Flaud, E. Perraudin, J. C. Wenger and E. Villenave, Gas- and particle-phase products from the photooxidation of acenaphthene and acenaphthylene by OH radicals, *Atmos. Environ.*, 2017, **151**, 34–44.

58 Y. Bedjanian, M. L. Nguyen and G. Le Bras, Kinetics of the reactions of soot surface-bound polycyclic aromatic hydrocarbons with the OH radicals, *Atmos. Environ.*, 2010, **44**, 1754–1760.

59 R. Atkinson and J. Arey, Atmospheric chemistry of gas-phase polycyclic aromatic hydrocarbons: formation of atmospheric mutagens, *Environ. Health Perspect.*, 1994, **102**, 117–126.

60 K. Ravindra, R. Sokhi and R. Vangrieken, Atmospheric polycyclic aromatic hydrocarbons: Source attribution, emission factors and regulation, *Atmos. Environ.*, 2008, **42**, 2895–2921.

61 Y. Yang, P. Guo, Q. Zhang, D. Li, L. Zhao and D. Mu, Seasonal variation, sources and gas/particle partitioning of polycyclic aromatic hydrocarbons in Guangzhou, China, *Sci. Total Environ.*, 2010, **408**, 2492–2500.

62 K.-H. Kim, S. A. Jahan, E. Kabir and R. J. C. Brown, A review of airborne polycyclic aromatic hydrocarbons (PAHs) and their human health effects, *Environ. Int.*, 2013, **60**, 71–80.

63 N.-D. Dat and M. B. Chang, Review on characteristics of PAHs in atmosphere, anthropogenic sources and control technologies, *Sci. Total Environ.*, 2017, **609**, 682–693.

64 A. Nel, Air Pollution–Related Illness Effect of Particles, *Science*, 2005, **308**, 804–805.

65 M. Riva, E. S. Robinson, E. Perraudin, N. M. Donahue and E. Villenave, Photochemical Aging of Secondary Organic Aerosols Generated from the Photooxidation of Polycyclic Aromatic Hydrocarbons in the Gas-Phase, *Environ. Sci. Technol.*, 2015, **49**, 5407–5416.

66 J. Arey, R. Atkinson, B. Zielinska and P. A. McElroy, Diurnal concentrations of volatile polycyclic aromatic hydrocarbons and nitroarenes during a photochemical air pollution episode in Glendora, California, *Environ. Sci. Technol.*, 1989, **23**, 321–327.

67 S. M. Platt, I. El Haddad, A. A. Zardini, M. Clairotte, C. Astorga, R. Wolf, J. G. Slowik, B. Temime-Roussel, N. Marchand, I. Ježek, L. Drinovec, G. Močnik, O. Möhler, R. Richter, P. Barmet, F. Bianchi, U. Baltensperger and A. S. H. Prévôt, Secondary organic aerosol formation from gasoline vehicle emissions in a new mobile environmental reaction chamber, *Atmos. Chem. Phys.*, 2013, **13**, 9141–9158.

68 A. T. Lambe, J. Zhang, A. M. Sage and N. M. Donahue, Controlled OH Radical Production via Ozone-Alkene Reactions for Use in Aerosol Aging Studies, *Environ. Sci. Technol.*, 2007, **41**, 2357–2363.

69 V. Kumar, J. G. Slowik, U. Baltensperger, A. S. H. Prevot and D. M. Bell, Time-Resolved Molecular Characterization of Secondary Organic Aerosol Formed from OH and NO_3 Radical Initiated Oxidation of a Mixture of Aromatic Precursors, *Environ. Sci. Technol.*, 2023, **57**, 11572–11582.

70 L. Stirnweis, C. Marcolli, J. Dommen, P. Barmet, C. Frege, S. M. Platt, E. A. Bruns, M. Krapf, J. G. Slowik, R. Wolf, A. S. H. Prévôt, U. Baltensperger and I. El-Haddad, Assessing the influence of NOx concentrations and

relative humidity on secondary organic aerosol yields from a-pinene photo-oxidation through smog chamber experiments and modelling calculations, *Atmos. Chem. Phys.*, 2017, **17**, 5035–5061.

71 P. Barmet, J. Dommen, P. F. DeCarlo, T. Tritscher, A. P. Praplan, S. M. Platt, A. S. H. Prévôt, N. M. Donahue and U. Baltensperger, OH clock determination by proton transfer reaction mass spectrometry at an environmental chamber, *Atmos. Meas. Tech.*, 2012, **5**, 647–656.

72 M. Taira and Y. Kanda, Continuous generation system for low-concentration gaseous nitrous acid, *Anal. Chem.*, 1990, **62**, 630–633.

73 M. Riva, M. Ehn, D. Li, S. Tomaz, F. Bourgain, S. Perrier and C. George, CI-Orbitrap: An Analytical Instrument To Study Atmospheric Reactive Organic Species, *Anal. Chem.*, 2019, **91**, 9419–9423.

74 D. Li, D. Wang, L. Caudillo, W. Scholz, M. Wang, S. Tomaz, G. Marie, M. Surdu, E. Eccli, X. Gong, L. Gonzalez-Carracedo, M. Granzin, J. Pfeifer, B. Rörup, B. Schulze, P. Rantala, S. Perrier, A. Hansel, J. Curtius, J. Kirkby, N. M. Donahue, C. George, I. El-Haddad and M. Riva, Ammonium CI-Orbitrap: a tool for characterizing the reactivity of oxygenated organic molecules, *Atmos. Meas. Tech.*, 2024, **17**, 5413–5428.

75 J. Krechmer, F. Lopez-Hilfiker, A. Koss, M. Hutterli, C. Stoermer, B. Deming, J. Kimmel, C. Warneke, R. Holzinger, J. Jayne, D. Worsnop, K. Fuhrer, M. Gonin and J. De Gouw, Evaluation of a New Reagent-Ion Source and Focusing Ion–Molecule Reactor for Use in Proton-Transfer-Reaction Mass Spectrometry, *Anal. Chem.*, 2018, **90**, 12011–12018.

76 A. Hansel, A. Jordan, R. Holzinger, P. Prazeller, W. Vogel and W. Lindinger, Proton transfer reaction mass spectrometry: on-line trace gas analysis at the ppb level, *Int. J. Mass Spectrom. Ion Processes*, 1995, **149–150**, 609–619.

77 R. S. Blake, P. S. Monks and A. M. Ellis, Proton-Transfer Reaction Mass Spectrometry, *Chem. Rev.*, 2009, **109**, 861–896.

78 M. Graus, M. Müller and A. Hansel, High resolution PTR-TOF: Quantification and formula confirmation of VOC in real time, *J. Am. Soc. Mass Spectrom.*, 2010, **21**, 1037–1044.

79 A. Jordan, S. Haidacher, G. Hanel, E. Hartungen, L. Märk, H. Seehauser, R. Schottkowsky, P. Sulzer and T. D. Märk, A high resolution and high sensitivity proton-transfer-reaction time-of-flight mass spectrometer (PTR-TOF-MS), *Int. J. Mass Spectrom.*, 2009, **286**, 122–128.

80 M. Riva, P. Rantala, J. E. Krechmer, O. Peräkylä, Y. Zhang, L. Heikkinen, O. Garmash, C. Yan, M. Kulmala, D. Worsnop and M. Ehn, Evaluating the performance of five different chemical ionization techniques for detecting gaseous oxygenated organic species, *Atmos. Meas. Tech.*, 2019, **12**, 2403–2421.

81 F. D. Lopez-Hilfiker, V. Pospisilova, W. Huang, M. Kalberer, C. Mohr, G. Stefenelli, J. A. Thornton, U. Baltensperger, A. S. H. Prevot and J. G. Slowik, An extractive electrospray ionization time-of-flight mass spectrometer (EESI-TOF) for online measurement of atmospheric aerosol particles, *Atmos. Meas. Tech.*, 2019, **12**, 4867–4886.

82 P. Eichler, M. Müller, B. D'Anna and A. Wisthaler, A novel inlet system for online chemical analysis of semi-volatile submicron particulate matter, *Atmos. Meas. Tech.*, 2015, **8**, 1353–1360.

83 M. Surdu, V. Pospisilova, M. Xiao, M. Wang, B. Mentler, M. Simon, D. Stolzenburg, C. R. Hoyle, D. M. Bell, C. P. Lee, H. Lamkaddam, F. Lopez-Hilfiker, L. R. Ahonen, A. Amorim, A. Baccarini, D. Chen, L. Dada, J. Duplissy, H. Finkenzeller, X.-C. He, V. Hofbauer, C. Kim, A. Kürten, A. Kvashnin, K. Lehtipalo, V. Makhmutov, U. Molteni, W. Nie, A. Onnela, T. Petäjä, L. L. J. Quéléver, C. Tauber, A. Tomé, R. Wagner, C. Yan, A. S. H. Prevot, J. Dommen, N. M. Donahue, A. Hansel, J. Curtius, P. M. Winkler, M. Kulmala, R. Volkamer, R. C. Flagan, J. Kirkby, D. R. Worsnop, J. G. Slowik, D. S. Wang, U. Baltensperger and I. E. Haddad, Molecular characterization of ultrafine particles using extractive electrospray time-of-flight mass spectrometry, *Environ. Sci.: Atmos.*, 2021, **1**, 434–448.

84 K. E. Kautzman, J. D. Surratt, M. N. Chan, A. W. H. Chan, S. P. Hersey, P. S. Chhabra, N. F. Dalleska, P. O. Wennberg, R. C. Flagan and J. H. Seinfeld, Chemical Composition of Gas- and Aerosol-Phase Products from the Photooxidation of Naphthalene, *J. Phys. Chem. A*, 2010, **114**, 913–934.

85 J. Liu, S. Zhu, T. Guo, B. Jia, L. Xu, J. Chen and P. Cheng, Smog chamber study of secondary organic aerosol formation from gas- and particle-phase naphthalene ozonolysis, *Atmos. Environ.*, 2023, **294**, 119490.

86 M. Li, E. Karu, C. Brenninkmeijer, H. Fischer, J. Lelieveld and J. Williams, Tropospheric OH and stratospheric OH and Cl concentrations determined from CH4, CH3Cl, and SF6 measurements, *npj Clim. Atmos. Sci.*, 2018, **1**, 29.

87 V. Pospisilova, F. D. Lopez-Hilfiker, D. M. Bell, I. El Haddad, C. Mohr, W. Huang, L. Heikkinen, M. Xiao, J. Dommen, A. S. H. Prevot, U. Baltensperger and J. G. Slowik, On the fate of oxygenated organic molecules in atmospheric aerosol particles, *Sci. Adv.*, 2020, **6**, eaax8922.

88 R. Atkinson and J. Arey, Mechanisms of the gas-phase reactions of aromatic hydrocarbons and PAHs with OH and NO3 radicals, *Polycyclic Aromat. Compd.*, 2007, **27**, 15–40.

89 A. Shiroudi and M. S. Deleuze, Theoretical Study of the Oxidation Mechanisms of Naphthalene Initiated by Hydroxyl Radicals: The H Abstraction Pathway, *J. Phys. Chem. A*, 2014, **118**, 3625–3636.

90 A. Shiroudi, M. S. Deleuze and S. Canneaux, Theoretical Study of the Oxidation Mechanisms of Naphthalene Initiated by Hydroxyl Radicals: The OH-Addition Pathway, *J. Phys. Chem. A*, 2014, **118**, 4593–4610.

91 H. J. (Julie) Lee, P. K. Aiona, A. Laskin, J. Laskin and S. A. Nizkorodov, Effect of Solar Radiation on the Optical Properties and Molecular Composition of Laboratory Proxies of Atmospheric Brown Carbon, *Environ. Sci. Technol.*, 2014, **48**, 10217–10226.

92 C. P. Lee, M. Surdu, D. M. Bell, H. Lamkaddam, M. Wang, F. Ataei, V. Hofbauer, B. Lopez, N. M. Donahue, J. Dommen, A. S. H. Prevot, J. G. Slowik, D. Wang, U. Baltensperger and I. El Haddad, Effects of aerosol size and coating thickness on the molecular detection using extractive electrospray ionization, *Atmos. Meas. Tech.*, 2021, **14**, 5913–5923.

93 D. M. Bell, J. Zhang, J. Top, S. Bogler, M. Surdu, J. G. Slowik, A. S. H. Prevot and I. El Haddad, Sensitivity Constraints of Extractive Electrospray for a Model System and Secondary Organic Aerosol, *Anal. Chem.*, 2023, **95**, 13788–13795.

94 D. E. Romonosky, N. N. Ali, M. N. Saiduddin, M. Wu, H. J. (Julie) Lee, P. K. Aiona and S. A. Nizkorodov, Effective absorption cross sections and photolysis rates of anthropogenic and biogenic secondary organic aerosols, *Atmos. Environ.*, 2016, **130**, 172–179.

95 O. Peräkylä, T. Berndt, L. Franzon, G. Hasan, M. Meder, R. R. Valiev, C. D. Daub, J. G. Varelas, F. M. Geiger, R. J. Thomson, M. Rissanen, T. Kurtén and M. Ehn, Large Gas-Phase Source of Esters and Other Accretion Products in the Atmosphere, *J. Am. Chem. Soc.*, 2023, **145**, 7780–7790.

96 C. M. Kenseth, N. J. Hafeman, S. P. Rezgui, J. Chen, Y. Huang, N. F. Dalleska, H. G. Kjaergaard, B. M. Stoltz, J. H. Seinfeld and P. O. Wennberg, Particle-phase accretion forms dimer esters in pinene secondary organic aerosol, *Science*, 2023, **382**, 787–792.

97 A. P. Bateman, S. A. Nizkorodov, J. Laskin and A. Laskin, Photolytic processing of secondary organic aerosols dissolved in cloud droplets, *Phys. Chem. Chem. Phys.*, 2011, **13**, 12199.

98 M. W. Alton, H. J. Stark, M. R. Canagaratna and E. C. Browne, Generalized Kendrick analysis for improved visualization of atmospheric mass spectral data, *Atmos. Meas. Tech.*, 2023, **16**, 3273–3282.

99 V. Lannuque and K. Sartelet, Development of a detailed gaseous oxidation scheme of naphthalene for secondary organic aerosol (SOA) formation and speciation, *Atmos. Chem. Phys.*, 2024, **24**, 8589–8606.

100 P. Khare, N. Kumar, K. M. Kumari and S. S. Srivastava, Atmospheric formic and acetic acids: An overview, *Rev. Geophys.*, 1999, **37**, 227–248.

101 J. H. Seinfeld and S. N. Pandis, *Atmospheric Chemistry and Physics: From Air Pollution to Climate Change*, Wiley, 2016.

102 L. Xu, M. M. Coggon, C. E. Stockwell, J. B. Gilman, M. A. Robinson, M. Breitenlechner, A. Lamplugh, J. D. Crounse, P. O. Wennberg, J. A. Neuman, G. A. Novak, P. R. Veres, S. S. Brown and C. Warneke, Chemical ionization mass spectrometry utilizing ammonium ions (NH_4^+ CIMS) for measurements of organic compounds in the atmosphere, *Atmos. Meas. Tech.*, 2022, **15**, 7353–7373.

103 Y. Li, U. Pöschl and M. Shiraiwa, Molecular corridors and parameterizations of volatility in the chemical evolution of organic aerosols, *Atmos. Chem. Phys.*, 2016, **16**, 3327–3344.